

Prompt Guidance and Human Proximal Perception for HOT Prediction with Regional Joint Loss

Yuxiao Wang¹ Yu Lei² Zhenao Wei¹ Weiyang Xue¹
Xinyu Jiang¹ Nan Zhuang³ Qi Liu^{1*}

¹South China University of Technology ²Southwest Jiaotong University ³Zhejiang University
{ftwangyuxiao, drliuqi}@scut.edu.cn

Abstract

The task of Human-Object conTact (HOT) detection involves identifying the specific areas of the human body that are touching objects. Nevertheless, current models are restricted to just one type of image, often leading to too much segmentation in areas with little interaction, and struggling to maintain category consistency within specific regions. To tackle this issue, a HOT framework, termed **P3HOT**, is proposed, which blends **Prompt** guidance and human **Proximal Perception**. To begin with, we utilize a semantic-driven prompt mechanism to direct the network’s attention towards the relevant regions based on the correlation between image and text. Then a human proximal perception mechanism is employed to dynamically perceive key depth range around the human, using learnable parameters to effectively eliminate regions where interactions are not expected. Calculating depth resolves the uncertainty of the overlap between humans and objects in a 2D perspective, providing a quasi-3D viewpoint. Moreover, a Regional Joint Loss (RJLoss) has been created as a new loss to inhibit abnormal categories in the same area. A new evaluation metric called “AD-Acc.” is introduced to address the shortcomings of existing methods in addressing negative samples. Comprehensive experimental results demonstrate that our approach achieves state-of-the-art performance in four metrics across two benchmark datasets. Specifically, our model achieves an improvement of **0.7↑**, **2.0↑**, **1.6↑**, and **11.0↑** in SC-Acc., mIoU, wIoU, and AD-Acc. metrics, respectively, on the HOT-Annotated dataset. Code is available at <https://github.com/YuxiaoWang-AI/P3HOT>.

1. Introduction

Human-Object conTact (HOT) prediction [5] originated from Human-Object Interaction (HOI) detection, an emerging advanced semantic understanding task [23, 25, 26].

*Corresponding author

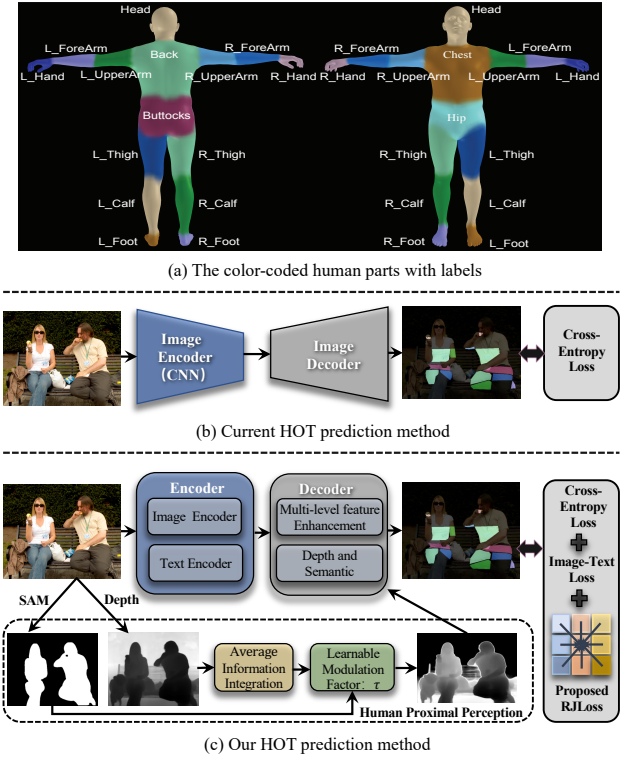


Figure 1. Current method vs Ours.

HOI focuses on detecting humans, objects, and their interactions. It does not specify which parts of the human body come into contact with objects. However, identifying specific contact points on the human is required in the HOT task. This technology has a wide range of possible uses and can be applied in various fields such as human-computer interaction [23], virtual reality [12], and gesture recognition [6], opening up new opportunities in these areas.

HOT divides into 18 categories (including background), namely, Head, Chest, L_UpperArm, L_ForeArm, L_Hand, R_UpperArm, R_ForeArm, Buttocks, R_Hand, Hip, Back, L_Thigh, L_Calf, L_Foot, R_Thigh, R_Calf, R_Foot, and background, as shown in Figure 1(a). Chen et al. [5] intro-

duced DHOT (using the encoder and decoder framework), which employed ResNet-50 as feature extraction network and designed a contact attention mechanism coupled with human masks for HOT prediction (Figure 1(b)). Nonetheless, DHOT only utilized features from the last layer of the feature extraction network, which can be disadvantageous for segmentation tasks that usually rely on low-level features to improve segmentation accuracy [6]. They predicted HOT from a single image modality, neglecting the guidance provided by other modalities. Additionally, the DHOT method failed to consider the consistency of classes within a region, leading to predictions that may include other classes within a particular class.

To overcome these challenges, we propose prompt guidance and human proximal perception method for HOT Prediction (a simplified diagram is shown in Figure 1(c)). Specifically, a text prompt mechanism is introduced to focus on human contact parts within the feature map. To filter out irrelevant information, a human proximal perception module is designed that utilizes a learnable parameter and human masks to dynamically perceive the depth range around the human. Furthermore, to regain initial texture detail loss during downsampling in the feature extraction stage, the lost image texture information is continuously refined by integrating outputs from each block of the feature extraction into the upsampling operations of the decoder. Finally, a novel loss function is designed, termed Regional Joint Loss (RJLoss), to ensure category consistency within regions and reduce the impact of abnormal categories.

Our contributions are summarized as follows:

- We are the first to integrate textual information into HOT, setting the stage for future research into multi-modal HOT.
- The proposed human proximal perception module is leveraged from a pseudo-3D perspective to assist HOT. A learnable threshold is used to dynamically perceive areas where interaction may exist, effectively reducing unnecessary interference.
- A novel loss function, i.e., Regional Joint Loss, is introduced to ensure intra-region category consistency. A new evaluation metric is suggested to overcome the shortcomings of current metrics when accounting for incorrect predictions.
- Extensive experiments have shown that our approach outperforms existing models on a newly introduced evaluation metric and achieves superior performance in SC-Acc., mIoU, and wIoU metrics on two benchmark datasets.

2. Related work

HOI detection. HOI focuses on detecting humans and objects and predicting the classification of interactions between humans and objects. Chao et al. [4] first proposed a

two-stage model using object detection and classification, in which a pre-trained detection model is initially employed to detect humans and objects, followed by a classification network to recognize interactions between them. However, the two-stage approach [4, 7, 8] decomposes the HOI task, leading to reduce efficiency. Therefore, Zou et al. [34] slightly modified the DETR [3] network, based on a transformer architecture, to detect humans, objects, and interactions simultaneously. It is categorized as a one-stage HOI method, which is more efficient [24, 30]. In addition, some researchers utilized the CLIP [21] to integrate text information into networks, further enhancing accuracy [15, 23].

HOT detection. Early HOT detection primarily focused on specific body parts such as hands and feet [6, 13, 17, 18, 22, 31, 33]. DRNet [18] combines Mask R-CNN [11] to learn hand localization and predict its contact state. The foot contact detection is often used to estimate body posture and joint angles [13, 33]. These methods lack a holistic perspective, failing to provide a comprehensive assessment of HOT. To address this, Tripathi et al. [22] proposed a human contact detection method based on 3D scenes. However, this method suffers from low computational efficiency in 3D environments. Then two datasets are constructed based on 2D perspectives: HOT-Annotated and HOT-Generated. [5]. DHOT introduced a combination of ResNet and convolutional attention mechanisms to achieve HOT predictions [5]. Later, PIHOT [27] was designed to address the human-object occlusion problem. PIHOT employs a restoration model and a depth model to recover object features. However, these methods do not consider category consistency within a region, leading to frequent occurrences of other categories within a specific category. Additionally, PIHOT does not explore multimodal information to enhance contact detection performance. Multimodal information, such as text prompts, has been proven effective in various tasks [15, 25, 26].

Why choose 2D over 3D contact detection? In many real-world applications, 2D tasks are sufficient for detecting HOT. For example, when understanding human-object interactions, it is sufficient to know whether the hands, feet, or other body parts are in contact with an object, without requiring precise 3D contact information. While 3D contact detection provides more information, it requires a larger number of parameters due to the complexity of 3D models, leading to slower speed. In contrast, 2D HOT detection is more suitable for some real-world applications. Moreover, 3D HOT detection datasets are currently scarce and challenging to construct. Although some recent works have attempted to create 3D HOT detection datasets [2, 22], the available data remains limited. These datasets are typically generated from existing 2D HOT datasets using the SMPL method [22], resulting in relatively coarse annotations for contact surfaces. Most importantly, 3D HOT de-

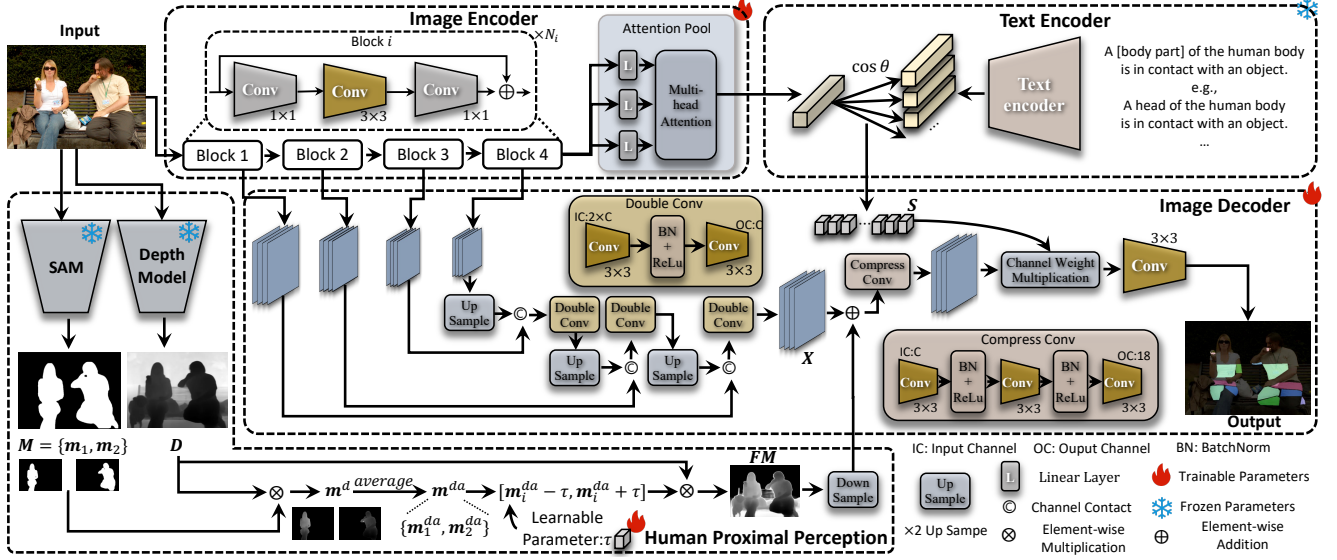


Figure 2. Overall architecture of the proposed P3HOT. The image encoder and text encoder are used to extract features from images and text, respectively. In the text encoder, we design a prompt template to create specific textual prompts. The similarity between the image and text features is computed to enhance the attention of the channel-specific feature maps in the image decoder. The human proximal perception module calculates the human mask and depth features for the input image, and uses learnable parameters, τ , to capture the depth range around the human body and surrounding environment. This module serves as a filter on the feature maps. The image decoder progressively refines the segmentation features by integrating each block output from the image encoder, incorporating both textual and depth modality features, to predict the final segmentation map.

tection datasets are only applicable to a limited range of objects [2], whereas 2D HOT datasets can be applied to a much broader variety of object categories [5].

3. Method

The proposed overall framework is illustrated in Figure 2. The image is first processed by an image encoder to extract features, while simultaneously, self-constructed textual prompts are processed by a text encoder to extract text features. Next, the image and text features are matched to influence the channels of the image features, thereby introducing attention based on textual modality information prompts. A human proximal perception mechanism is designed, where the human mask is combined with depth features containing pseudo-3D information to obtain the average depth of each human. Then a learnable parameter, τ , dynamically adjusts the depth range around each human, filtering out irrelevant noise regions. Additionally, to integrate fine-grained information within the feature extraction encoder, we continuously fuse features from each block of the image encoder during the decoding process. Finally, the HOT prediction map is obtained.

3.1. Image Encoder

The ResNet-50 with an attention pooling layer is used as our image encoder. Given an image I , each block of ResNet-50 outputs a feature map $F_i \in \mathbb{R}^{C_i \times \frac{H}{S_i} \times \frac{W}{S_i}}$,

where $i = \{1, 2, 3, 4\}$, the channel dimensions $C_i = \{256, 512, 1024, 2048\}$ and the downsample ratio of each block $S_i = \{4, 8, 16, 32\}$. To compute similarity with text features, we flatten F_4 into a one-dimensional vector through an attention pool to output $F_{IE} \in \mathbb{R}^{1 \times 1024}$. The attention pool, proposed by Radford et al. [21], is primarily designed to capture key information within the image and align it with textual descriptions for enhanced matching with text features.

3.2. Text Encoder

To extract text features, we first construct a text prompt template T , which takes the form: "A [body part] of the human body is in contact with an object." Here, [body part] is sequentially replaced with each of the 17 human body parts ("Head", "Chest", "Left Upper Arm", "Left Fore Arm", "Left Hand", "Right Upper Arm", "Right Fore Arm", "Buttocks", "Right Hand", "Hip", "Back", "Left Thigh", "Left Calf", "Left Foot", "Right Thigh", "Right Calf", "Right Foot") mentioned earlier. After encoding, we obtain $F_{TE} \in \mathbb{R}^{TN \times 1024}$, where TN denotes the number of constructed text. The text encoder is initialized using the model proposed by Radford et al. [21], freezing its parameters during training. The similarity $S \in \mathbb{R}^{1 \times TN}$ between $F_{IE} \in \mathbb{R}^{1 \times 1024}$ and $F_{TE} \in \mathbb{R}^{TN \times 1024}$ is then computed, via:

$$S = \frac{\mathbf{F}_{IE} \cdot \mathbf{F}_{TE}^T}{\|\mathbf{F}_{IE}\| \cdot \|\mathbf{F}_{TE}\|}. \quad (1)$$

Since we train the image encoder while keeping the text encoder frozen, the two would quickly become misaligned without an image-text similarity loss constraint. Therefore, after S , we compute the loss with the ground truth to further update the image encoder parameters, ensuring alignment with the text encoder and preventing conflicts.

3.3. Human Proximal Perception

This module aims to preserve humans and the environment around them by eliminating irrelevant backgrounds. To accomplish this, the initial step is calculating the average depth for each person. Then, the depth range around each person is determined based on the learnable parameter τ to dynamically select the appropriate target region. Specifically, the improved SAM model is used to generate humans masks M based on the text prompt “person” [19], and apply the ZoeDepth model [1] to extract the depth features $D \in \mathbb{R}^{H \times W}$ of the input image. Here, $M = \{m_1, m_2, \dots, m_N\}$, where $m_i \in \mathbb{R}^{H \times W}$ represents the i -th human mask. In m_i , 0 indicates the background, and 1 represents the human body. N denotes the total number of persons. Next, we obtain the average depth of each human based on M and D as follows:

$$D_{Norm} = \frac{D - \text{Min}(D)}{\text{Max}(D) - \text{Min}(D)}, \quad (2)$$

$$m_i^d = m_i \otimes D_{Norm}, i = 1, 2, \dots, N, \quad (3)$$

$$m_i^{da} = \frac{\sum_{h=1}^H \sum_{w=1}^W m_i^d[h, w]}{\sum_{h=1}^H \sum_{w=1}^W m_i[h, w]}, \quad (4)$$

where \otimes represents element-wise multiplication. Eq. 2 is used to normalize D within the range $[0, 1]$, Min and Max denote the minimum and maximum values, respectively. m_i^d represents the depth matrix of the i -th human, and m_i^{da} denotes the average depth value for i -th human. Subsequently, based on the learned parameter τ , we obtain the depth range d^r via:

$$d_i^r = \{[m_i^{da} - \tau, m_i^{da} + \tau] | i = 1, 2, \dots, N\}. \quad (5)$$

Next, d^r is used to generate a filter mask matrix $FM \in \mathbb{R}^{H \times W}$, which is composed only of 0 and 1, to retain the valid regions of the human and surrounding objects. That is:

$$FM = \begin{bmatrix} a_{11} & a_{12} & \cdots & a_{1W} \\ a_{21} & a_{22} & \cdots & a_{2W} \\ \vdots & \vdots & \ddots & \vdots \\ a_{H1} & a_{H2} & \cdots & a_{HW} \end{bmatrix}_{H \times W} = [a_{pq}], \quad (6)$$

$$a_{pq} = \begin{cases} 1, & \text{if } m_i^{da} - \tau < D_{Norm}^{pq} < m_i^{da} + \tau, \\ 0, & \text{otherwise,} \end{cases} \quad (7)$$

where p and q represent the element indices at the p -th row and q -th column of the matrix. FM will be downsampled and added with the feature map X from the image decoder, thereby highlighting the human body and its surrounding regions. However, since FM is generated through a comparison operation that directly assigns elements to 0 or 1, it is not a continuous function, and thus, it cannot be back-propagated, meaning the parameter τ cannot be updated. To address this, we propose an alternative solution as follows:

$$FM = \begin{bmatrix} 0 & 0 & \cdots & 0 \\ 0 & 0 & \cdots & 0 \\ \vdots & \vdots & \ddots & \vdots \\ 0 & 0 & \cdots & 0 \end{bmatrix}_{H \times W}, \quad (8)$$

$$\Theta_i = (D_{Norm} - (m_i^{da} - \tau)) \otimes ((m_i^{da} + \tau) - D_{Norm}), \quad (9)$$

$$FM = FM + \sum_{i=1}^N \text{ReLU}(\Theta_i), \quad (10)$$

$$O = \text{DS}(FM) \oplus X. \quad (11)$$

Eq. 9 converts the depth values within the specified range to positive values, while those outside the range are set to negative values. The ReLU function in Eq. 10 keeps the original positive values and turns the negative values into zeros. Since the ReLU function is differentiable, it allows the parameter τ to be updated during backpropagation. DS denotes the downsampling operation, which reduces the size of FM from $H \times W$ to $\frac{H}{4} \times \frac{W}{4}$. \oplus represents element-wise addition.

3.4. Image Decoder

After extracting the features in Sec. 3.1, it is necessary to continually upsample them to create the segmentation map. In the image encoder, the input image is continuously downsampled, resulting in a gradual loss of image details. Thus, when upsampling, it is necessary to combine the results F from the less deep blocks in the encoder network in order to regain missing details like image textures $X \in \mathbb{R}^{256 \times \frac{H}{4} \times \frac{W}{4}}$, via:

$$x_4 = F_4,$$

$$x_{i-1} = \text{DoubleConv}(\text{Up}(x_i) \textcircled{\hspace{0.1cm}} F_{i-1}), i = 4, 3, 2,$$

$$X = x_1, \quad (12)$$

where $\textcircled{\hspace{0.1cm}}$ denotes channel concatenation. Subsequently, the features X are processed through Eq. 11 to obtain O , focusing solely on the human and the surrounding area of human within a certain range. To focus on the text input,

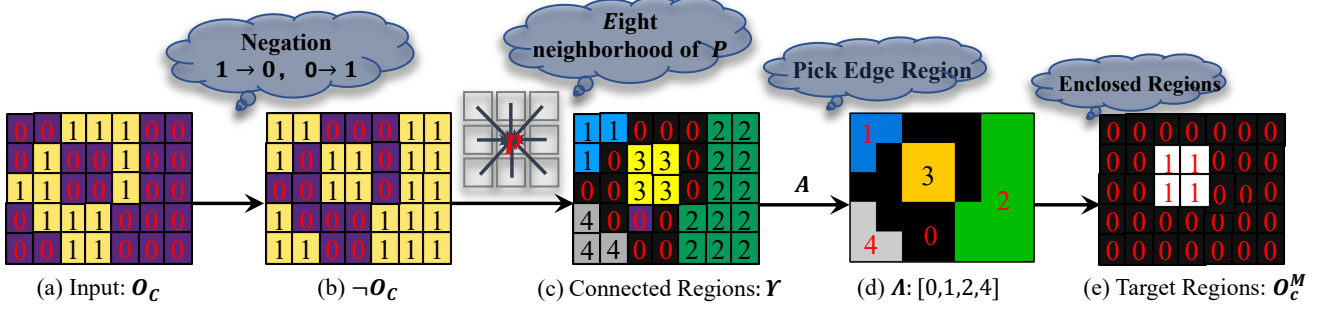


Figure 3. The calculation schematic of regions of other categories enclosed within category c . First, the input matrix values equal to c are set to 1, while all other values are set to 0, forming the input O_c as shown in subfigure (a). Then, O_c is inverted to obtain $\neg O_c$. The connected regions of $\neg O_c$ are computed, resulting in Υ . Next, the values from the first and last rows and columns of Υ are extracted, forming the set $\Lambda = \{0, 1, 2, 4\}$. Since the value 3 is missing in Λ , we set all elements in Υ that are equal to 3 to 1 and the rest to 0, yielding O_c^M . The region in O_c^M where elements are 1 represents the area of other categories enclosed within category c .

Compress Conv initially reduces the channels of O to 18 before combining them using the equation below:

$$O = \text{Compress Conv}(O),$$

$$O[i] = \begin{cases} O[i] \times 1, & \text{if } i = 18 \\ O[i] \times S[i], & \text{if } i = 1, 2, \dots, 17, \end{cases} \quad (13)$$

where $O[i]$ represents the background feature map based on channel dimension when i is 18. We keep the background feature map unchanged and adjust the remaining channels based on S . Finally, O is passed through the convolution layers to obtain the final segmentation map $O \in \mathbb{R}^{18 \times \frac{H}{4} \times \frac{W}{4}}$. It is not difficult to observe that the output of the network, O , does not have a dimension of $18 \times H \times W$, but instead undergoes a $4 \times$ downsampling. This is because we also apply a $4 \times$ downsampling to the ground truth ($GT \in \mathbb{R}^{\frac{H}{4} \times \frac{W}{4}}$), which is consistent with DHOT [5] and PIHOT [27].

3.5. Loss

HOT categorizes the areas of contact between humans and objects into 18 classes, which include the background. Current techniques that utilize cross-entropy loss frequently produce segmentation outcomes that contain inaccurate categories in specific regions of the resultant map. To tackle this problem, we create a Regional Joint Loss, known as RJLoss. RJLoss is made up of two parts: Local Joint Loss and Global Joint Loss.

Local Joint Loss. Initially, we utilize the ground truth (GT) to isolate regions specific to each class. If there are additional classes present in a region, the loss for that region is adjusted accordingly. Specifically, the Local Joint Loss for a given class c is defined as:

$$O_c(\text{ or } GT_c) = \{o_{pq}(\text{ or } gt_{pq}) | p, q = 1, 2, \dots, \frac{H(W)}{4}\},$$

$$o_{pq}(\text{ or } gt_{pq}) = \begin{cases} 1, & \text{if } o_{pq}(\text{ or } gt_{pq}) = c \\ 0, & \text{otherwise} \end{cases}, \quad (14)$$

$$\mathcal{L}_c^L = \frac{\sum(|O_c - GT_c| \otimes GT_c)}{\sum GT_c}, \quad (15)$$

where $|\cdot|$ denotes the absolute value. In Eq. 15, $|O_c - GT_c|$ sets the parts where O_c equals GT_c to 0 and the parts where they differ to 1. The $|O_c - GT_c| \otimes GT_c$ identifies cases where other classes appear within class c . The symbol \sum denotes the summation over all elements of the matrix. Subsequently, the Local Joint Loss for all classes is defined as:

$$\mathcal{L}^L = \sum_{c=1}^{18} \mathcal{L}_c^L \quad (16)$$

Global Joint Loss. The Local Joint Loss aims to eliminate classes from the target class region that do not belong there, as determined by the GT . However, it fails to consider the entire prediction map, including non-contact areas of the human body. The Global Joint Loss calculates the joint loss over the entire prediction map. First, we need to identify the connected regions of class c and compute the regions of other classes enclosed within them (the simplified schematic diagram is shown in Figure 3(a), (b), (c) and (d)) using

$$A = [a_{ij}] = \begin{pmatrix} 1 & \dots & 1 \\ \vdots & 0 & \vdots \\ 1 & \dots & 1 \end{pmatrix}_{\frac{H}{4} \times \frac{W}{4}},$$

$$\Upsilon = \text{ConnectedArea}(\neg O_c),$$

$$\Lambda = \{\Upsilon_{ij} | \forall i, j \in [1, \frac{H}{4}], [1, \frac{W}{4}] \text{ and } a_{ij} = 1\}, \quad (17)$$

where A represents a matrix with boundaries set to 1 and the interior set to 0, and \neg denotes the negation operation on the matrix, flipping 0 to 1 and 1 to 0 (as illustrated in

Figure 3(a) and (b)). ConnectedArea is a function for finding connected regions, implemented using the built-in functions from the scipy library. It detects all connected regions in the matrix and assigns a unique label to each region (as illustrated in Figure 3(c)). Specifically, it iterates over all elements in the input matrix, searching in 8 directions (up, down, left, right, top-left, bottom-left, top-right, bottom-right) for values equal to the target element, and marks them as a connected region. Λ denotes several unequal region labels extracted from the boundary of the Υ through \mathbf{A} (as shown in Figure 3(d)). Then the connected regions are identified not in Λ (as shown in Figure 3(e)) using the following formula, which gives us the target regions enclosed by contact class c .

$$\begin{aligned} \mathbf{O}_c^M &= [m_{ij}] \\ m_{ij} &= \begin{cases} 1, & \text{if } \Upsilon_{ij} \notin \Lambda \\ 0, & \text{otherwise} \end{cases}. \end{aligned} \quad (18)$$

Then, the internal error class loss is calculated based on \mathbf{O}_c^M :

$$\mathcal{L}_c^G = \sum (-\mathbf{O}_c \otimes \mathbf{O}_c^M). \quad (19)$$

The Global Joint Loss for all classes is defined as:

$$\mathcal{L}^G = \sum_{c=1}^{18} \mathcal{L}_c^G. \quad (20)$$

The overall network loss is optimized jointly using cross-entropy and RJLoss. Additionally, a basic image-text matching loss is incorporated to co-optimize the image encoder. The total loss is defined as:

$$\mathcal{L} = \text{CE}(\mathbf{O}, \mathbf{GT}) + \alpha \mathcal{L}^L + \beta \mathcal{L}^G + \gamma \text{BE}(\mathbf{S}, \mathbb{C}), \quad (21)$$

where CE and BE denote the cross-entropy loss and the binary cross-entropy loss, respectively. Both the image and text encoders are initialized with CLIP. We freeze the text encoder and train the image encoder using BE, enabling the image and text encoders to operate collaboratively. $\mathbf{S} \in \mathbb{R}^{1 \times 18}$ represents the image-text matching similarity, and $\mathbb{C} \in \mathbb{R}^{1 \times 18}$ indicates the contact classes present in the input image. If class c appears in the image, then $\mathbb{C}_c = 1$; otherwise, $\mathbb{C}_c = 0$.

4. Experiment

4.1. Datasets

To assess the performance of the proposed approach, two benchmark datasets, HOT-Annotated and HOT-Generated, are employed. The HOT-Annotated comprises 15,082 images with 67,088 contact areas from V-COCO [9], HAKE [14], and Watch-n-Patch [28]. The HOT-Generated dataset is constructed by using the PROX [10] and SMPL-X [20] frameworks, featuring 20,205 images and a total of 95,179 contact areas.

4.2. Setup

For a fair comparison, ResNet-50 is used as the backbone of the image encoder module. In Eq. 21, α , β , and γ are set to 0.3, 0.1, and 1.0, respectively. The network is optimized using the AdamW optimizer. The batch size is set to 4 per GPU. The experimental environment is Ubuntu 20.04, equipped with 8 NVIDIA A6000 (48GB) GPUs. PyTorch version is 1.11.0, torchvision version is 0.12.0, and Python is 3.8.19.

4.3. Metrics

HOT was proposed in 2023 by Chen et al. [5], and it includes four evaluation metrics: SC-Acc., C-Acc., mIoU, and wIoU. SC-Acc. represents the proportion of correctly classified pixels. C-Acc. denotes the accuracy of classifying pixels on the human body, which is a binary classification. mIoU measures the Intersection over Union between the predicted and ground truth regions, while wIoU is the weighted IoU across all classes. To adjust mIoU and wIoU to the same numerical range as SC-Acc. and C-Acc., i.e., 0-100, we multiply mIoU and wIoU by 100.

We found that the C-Acc. metric has some issues (see **supplementary materials for details**). If the prediction map classifies the entire image as a contact class, C-Acc. would be 100% because the predicted region encompasses the entire human body. This outcome is clearly undesirable, as most of the prediction pixels are incorrect in this case. To address this issue, we propose a new evaluation metric to replace C-Acc., called Adaptive Accuracy (AD-Acc.). We first extract the channel indices with the maximum values from the prediction map, resulting in a new $\mathbf{O} \in \mathbb{R}^{\frac{H}{4} \times \frac{W}{4}}$, where each element represents the predicted class. The calculation of AD-Acc. is then defined as follows:

$$\begin{aligned} \mathbf{GT}^B (\text{ or } \mathbf{O}^B) &= [gt_{ij}] (\text{ or } [o_{ij}]) \\ &= \begin{cases} 1, & \text{if } gt_{ij} (\text{ or } o_{ij}) > 0 \\ 0, & \text{otherwise} \end{cases}, \end{aligned} \quad (22)$$

$$\boldsymbol{\zeta} = \mathbf{M} - \mathbf{GT}^B \otimes \mathbf{M}, \quad (23)$$

$$\text{AD-Acc.} = \frac{\sum (\mathbf{GT}^B \otimes \mathbf{O}^B)}{\sum \mathbf{GT}^B + \delta} - \frac{\sum (\boldsymbol{\zeta} \otimes \mathbf{O}^B)}{\sum \boldsymbol{\zeta} + \delta}, \quad (24)$$

where \mathbf{GT}^B and \mathbf{O}^B denote the binarized of \mathbf{GT} and \mathbf{O} , respectively. \mathbf{M} represents the human mask. $\boldsymbol{\zeta}$ refers to the negative samples selected based on the human mask, specifically the parts of the human body excluding the ground truth. δ is set to 1e-6. AD-Acc. takes into account both positive and negative samples, balancing cases where human classification errors occur, making it a more robust evaluation metric.

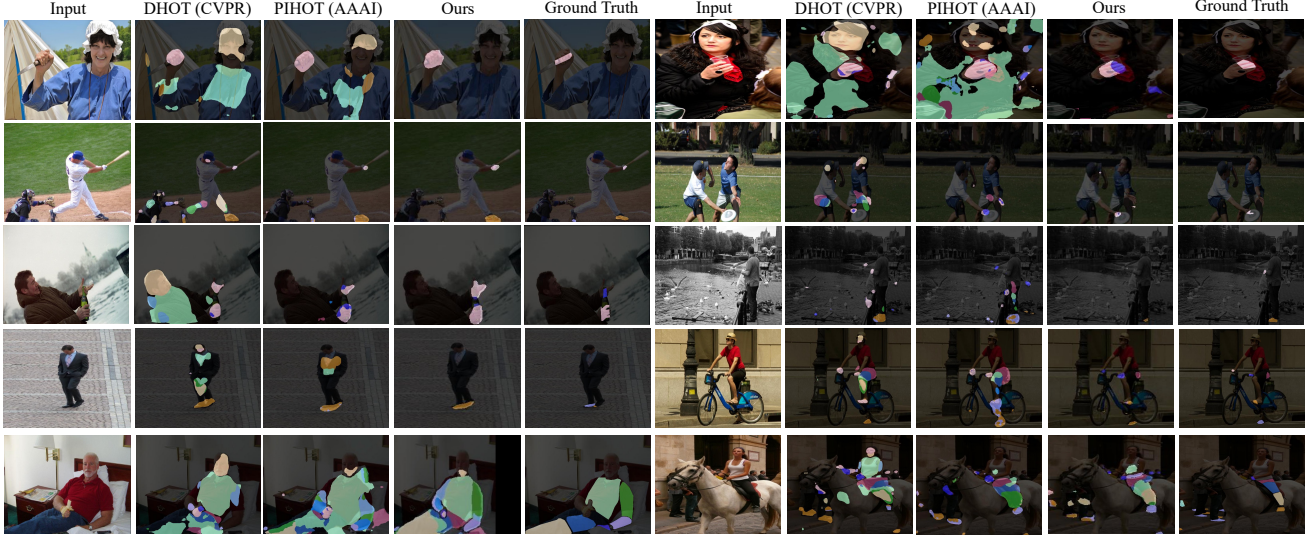


Figure 4. Visualization of DHOT [5], PIHOT [27], and our proposed method.

Model	HOT-Annotated					HOT-Generated				
	SC-Acc.	C-Acc.	mIoU	wIoU	AD-Acc.	SC-Acc.	C-Acc.	mIoU	wIoU	AD-Acc.
ResNet+UperNet [29]	35.1	62.6	19.5	22.7	-	21.1	42.7	8.0	11.6	-
ResNet+PPM [32]	34.6	61.1	20.1	23.3	-	21.2	41.1	7.5	11.9	-
DHOT(ResNet-50) _{wo/att} [5]	24.1	42.8	14.8	18.7	-	12.0	24.6	5.1	9.9	-
DHOT(ResNet-50) _{pure_att} [5]	33.8	58.4	18.9	23.7	-	20.3	40.1	7.7	11.3	-
DHOT(ResNet-50) _{Full} [5]	40.7	70.7	21.5	26.0	-	30.4	54.3	13.9	16.7	-
DHOT(ResNet-50) _{Full} -OF [5]	40.1	69.2	22.1	25.0	31.0	24.3	59.2	12.0	13.0	24.9
PIHOT(ResNet-50) [27]	45.3	80.7	23.6	28.6	31.3	34.9	76.3	16.9	21.2	25.4
Ours(ResNet-50)	46.0	74.9	25.6	30.2	42.3	35.2	70.8	18.0	23.1	30.6

* -OF indicates the optimal result provided by themselves in Github.

Table 1. Performance comparisons on HOT-Annotated and HOT-Generated datasets.

4.4. Performance

The experimental results (Table 1) demonstrate that our proposed model significantly outperforms all other models on both HOT-Annotated and HOT-Generated datasets across four evaluation metrics. For example, on the HOT-Annotated dataset, our model achieves a SC-Acc. of 46.0, which is notably higher than PIHOT at 45.3 and DHOT(ResNet-50)_{Full}-OF at 40.1. Similarly, for mIoU, our model scores 25.6 compared to PIHOT at 23.6 and DHOT(ResNet-50)_{Full}-OF at 22.1. Although our method is 5.8 points lower than PIHOT in terms of C-Acc., we previously mentioned that C-Acc. is not an accurate metric for evaluating the HOT task. This is because if every pixel in the entire image is predicted as a single contact category, C-Acc. would be 100, which is clearly not the desired outcome. To address this limitation, we propose a new evaluation metric, AD-Acc. In terms of AD-Acc., our method outperforms PIHOT by 11.0. On the HOT-Generated dataset, our model achieves a AD-Acc. of 30.6,

surpassing PIHOT at 25.4 and DHOT(ResNet-50)_{Full}-OF at 24.9. These substantial improvements emphasize the effectiveness of our approach and the critical role of fully integrated various mechanisms in achieving superior performance for HOT prediction tasks. **Use more powerful encoder results, such as Swin-L [16]. See supplementary materials. In the supplementary materials, we include additional test results of the model, such as different encoders, inference time, and more.**

4.5. Ablation Study

Various components. In Table 2, all experiments were conducted using only cross-entropy loss to train the network model, with α , β , and γ all set to 0. The baseline refers to using only the image encoder and image decoder, where the decoder directly performs convolution and prediction on the features from the last layer of the encoder. +Fine denotes refining features by combining the output of each block from the encoder during upsampling in the image decoder, preventing the loss of low-level texture information. +TE indi-

cates the inclusion of the text encoder module. +HPP represents the addition of the human proximal perception module. It is evident that as more components are added, the performance of the proposed method continues to improve.

	SC-Acc.	C-Acc.	mIoU	wIoU	AD-Acc.
baseline	37.2	65.9	19.0	22.9	30.3
+Fine	38.9	68.4	20.1	24.5	34.1
+TE	40.3	69.6	21.0	25.9	37.1
+HPP	43.2	71.8	23.1	27.7	38.9

Table 2. Ablation experiments of adding various components on HOT-Annotated.

Different loss. The impact of adding different loss functions on the experimental results is listed in Table 3. CE denotes using only cross-entropy loss. +BE indicates the addition of binary cross-entropy loss on CE. +RJLoss represents further incorporation of the Regional Joint Loss proposed in this paper. By introducing the text modality and optimizing with BE, the performance improves. After adding RJLoss, the optimal results are achieved, with a significant performance boost.

	SC-Acc.	C-Acc.	mIoU	wIoU	AD-Acc.
CE	43.2	71.8	23.1	27.7	38.9
+BE	44.5	72.3	23.8	28.3	40.1
+RJLoss	46.0	74.9	25.6	30.2	42.3

Table 3. Impact of different loss functions on performance.

The range of D . The depth map is used to adaptively select the depth around the human body based on the human mask and the learnable parameter τ . The τ is influenced by the range of the depth map. The performance of normalized and non-normalized depth maps are compared, as shown in Table 4, where R denotes real numbers. When the range of D is unconstrained, different input images have varying depths, making it difficult to optimize τ within a specific interval, resulting in lower performance. After normalizing D , the results reached the optimal performance.

	SC-Acc.	C-Acc.	mIoU	wIoU	AD-Acc.
$D \in R$	44.1	72.4	24.3	28.1	40.2
$D \in [0, 1]$	46.0	74.9	25.6	30.2	42.3

Table 4. Performance comparison of depth map D Range.

Different loss weights. The impact of different loss weights on performance is listed in Table 5. When α , β , and γ are all set to 1.0, the performance is significantly reduced. We observed that the early values of \mathcal{L}^L and \mathcal{L}^G are quite large, causing the model to overlook the original segmentation task and instead focus excessively on the presence of other classes within regions. Consequently, as α and β decrease, the model’s performance gradually improves,

achieving optimal results at $\alpha = 0.3$ and $\beta = 0.5$. A similar situation occurs with the BE (binary cross-entropy) loss. If γ is too large, the focus of the method shifts away, whereas if γ is too small, the image-text accuracy is neglected.

α	β	γ	SC-Acc.	C-Acc.	IoU	mIoU	AD-Acc.
1.0	1.0	1.0	42.3	71.9	23.1	27.7	40.1
0.5	0.5	1.0	44.3	72.9	24.2	28.7	41.4
0.3	0.3	1.0	44.1	73.4	24.8	29.0	41.5
0.3	0.1	1.0	46.0	74.9	25.6	30.2	42.3
0.3	0.1	0.5	45.5	73.8	24.9	29.2	41.7
0.3	0.1	2.0	44.7	72.7	23.8	28.9	41.5

Table 5. Effect of different loss weights on performance.

4.6. Visualization

We also provide qualitative visualizations to evaluate the effectiveness of our method. In Figure 4, DHOT [5] represents a CVPR 2023 method, while PIHOT [27] is the latest state-of-the-art (SOTA) approach, accepted at AAAI 2025. It is evident that our proposed method aligns closely with the ground truth. The discrepancy between DHOT’s results and the actual scene is particularly noticeable. Specifically, when evaluating individuals holding a knife, baseball players, and a woman drinking water (top three rows), DHOT’s predictions significantly deviate from the actual interactions.

Similarly, PIHOT produces poor results in certain cases, such as the second sample in the first row and the first sample in the last row. The primary reason for this issue is that PIHOT fails to enforce category consistency within a region, leading to frequent misclassification errors. In contrast, our framework refines predictions through progressive upsampling and utilizes depth information to locate areas around the human body, suppressing irrelevant regions outside the body. Furthermore, by optimizing with RJLoss, our approach better focuses on contact areas and ensures category consistency across the entire region. **For more detailed visualizations, please refer to the supplementary materials.**

5. Conclusion

This paper introduces a prompt guidance and human proximal perception method for HOT prediction (P3HOT). To enhance the performance of models that utilize only one type of image, prompt guidance are being used for the first time to help the network focus more on human body contact areas. Additionally, a human proximal perception mechanism is employed to dynamically perceive key depth information around the human body based on learnable parameters, excluding areas where interactions are improbable. In the decoder, features are gradually combined during upsampling to improve segmentation boundaries and restore initial

texture details. Importantly, a new loss function named Regional Joint Loss is presented to maintain the consistency of categories within regions and reduce abnormal categories. Extensive experiments have shown that our model outperforms existing models on newly designed evaluation metrics and achieves state-of-the-art performance in SC-Acc., mIoU, and wIoU metrics on two benchmark datasets.

6. Acknowledgments

This work was supported in part by the National Natural Science Foundation of China under Grant 62202174, in part by the GJYC program of Guangzhou under Grant 2024D01J0081, in part by the ZJ program of Guangdong under Grant 2023QN10X455, in part by The Taihu Lake Innovation Fund for the School of Future Technology of South China University of Technology under Grant 2024B105611004, and in part by the Guangdong Provincial Key Laboratory of Human Digital Twin (2022B1212010004).

References

- [1] Shariq Farooq Bhat, Reiner Birkel, Diana Wofk, Peter Wonka, and Matthias Müller. ZoeDepth: Zero-shot transfer by combining relative and metric depth. *arXiv preprint arXiv:2302.12288*, 2023. 4
- [2] Bharat Lal Bhatnagar, Xianghui Xie, Ilya A Petrov, Cristian Sminchisescu, Christian Theobalt, and Gerard Pons-Moll. Behave: Dataset and method for tracking human object interactions. In *Proceedings of the IEEE/CVF Conference on Computer Vision and Pattern Recognition*, pages 15935–15946, 2022. 2, 3
- [3] Nicolas Carion, Francisco Massa, Gabriel Synnaeve, Nicolas Usunier, Alexander Kirillov, and Sergey Zagoruyko. End-to-end object detection with transformers. In *Proceedings of the European Conference on Computer Vision (ECCV)*, pages 213–229. Springer, 2020. 2
- [4] Yu-Wei Chao, Yunfan Liu, Xieyang Liu, Huayi Zeng, and Jia Deng. Learning to detect human-object interactions. In *2018 IEEE Winter Conference on Applications of Computer Vision (WACV)*, pages 381–389, 2018. 2
- [5] Yixin Chen, Sai Kumar Dwivedi, Michael J Black, and Dimitrios Tzionas. Detecting human-object contact in images. In *Proceedings of the IEEE/CVF Conference on Computer Vision and Pattern Recognition*, pages 17100–17110, 2023. 1, 2, 3, 5, 6, 7, 8
- [6] Zhenchao Cui, Yu Lei, Yuxiao Wang, Wenzhu Yang, and Jing Qi. Hand gesture segmentation against complex background based on improved atrous spatial pyramid pooling. *Journal of Ambient Intelligence and Humanized Computing*, 14(9):11795–11807, 2023. 1, 2
- [7] Yiming Gao, Zhanghui Kuang, Guanbin Li, Wayne Zhang, and Liang Lin. Hierarchical reasoning network for human-object interaction detection. *IEEE Transactions on Image Processing*, 30:8306–8317, 2021. 2
- [8] Georgia Gkioxari, Ross Girshick, Piotr Dollár, and Kaiming He. Detecting and recognizing human-object interactions. In *Proceedings of the IEEE Conference on Computer Vision and Pattern Recognition*, pages 8359–8367, 2018. 2
- [9] Saurabh Gupta and Jitendra Malik. Visual semantic role labeling. *arXiv preprint arXiv:1505.04474*, 2015. 6
- [10] Mohamed Hassan, Vasileios Choutas, Dimitrios Tzionas, and Michael J Black. Resolving 3d human pose ambiguities with 3d scene constraints. In *Proceedings of the IEEE/CVF international conference on computer vision*, pages 2282–2292, 2019. 6
- [11] Kaiming He, Georgia Gkioxari, Piotr Dollár, and Ross Girshick. Mask R-CNN. In *Proceedings of the IEEE international conference on computer vision*, pages 2961–2969, 2017. 2
- [12] Gazi Karam Illahi, Ashutosh Vaishnav, Teemu Kämäräinen, Matti Siekkinen, and Mario Di Francesco. Learning to predict head pose in remotely-rendered virtual reality. In *Proceedings of the 14th Conference on ACM Multimedia Systems*, pages 27–38, 2023. 1
- [13] Yo Kobayashi and Yasutaka Nakashima. Estimation of posture and joint angle of human body using foot pressure distribution: Morphological computation with human foot. *arXiv preprint arXiv:2401.12464*, 2024. 2
- [14] Yong-Lu Li, Liang Xu, Xinpeng Liu, Xijie Huang, Yue Xu, Shiyi Wang, Hao-Shu Fang, Ze Ma, Mingyang Chen, and Cewu Lu. PastaNet: Toward human activity knowledge engine. In *Proceedings of the IEEE/CVF Conference on Computer Vision and Pattern Recognition*, pages 382–391, 2020. 6
- [15] Yue Liao, Aixi Zhang, Miao Lu, Yongliang Wang, Xiaobo Li, and Si Liu. GEN-VLKT: Simplify association and enhance interaction understanding for hoi detection. In *Proceedings of the IEEE/CVF Conference on Computer Vision and Pattern Recognition*, pages 20123–20132, 2022. 2
- [16] Ze Liu, Yutong Lin, Yue Cao, Han Hu, Yixuan Wei, Zheng Zhang, Stephen Lin, and Baining Guo. Swin transformer: Hierarchical vision transformer using shifted windows. In *Proceedings of the IEEE/CVF International Conference on Computer Vision*, pages 10012–10022, 2021. 7
- [17] Gyeongsik Moon, Shunsuke Saito, Weipeng Xu, Rohan Joshi, Julia Buffalini, Harley Bellan, Nicholas Rosen, Jesse Richardson, Mallorie Mize, Philippe De Bree, et al. A dataset of relighted 3d interacting hands. *Advances in Neural Information Processing Systems*, 36, 2024. 2
- [18] Supreeth Narasimhaswamy, Trung Nguyen, and Minh Hoai Nguyen. Detecting hands and recognizing physical contact in the wild. *Advances in neural information processing systems*, 33:7841–7851, 2020. 2
- [19] paulguerrero. Language segment-anything. <https://github.com/paulguerrero/lang-sam>, 2024. 4
- [20] Georgios Pavlakos, Vasileios Choutas, Nima Ghorbani, Timo Bolkart, Ahmed AA Osman, Dimitrios Tzionas, and Michael J Black. Expressive body capture: 3d hands, face, and body from a single image. In *Proceedings of the IEEE/CVF conference on computer vision and pattern recognition*, pages 10975–10985, 2019. 6

- [21] Alec Radford, Jong Wook Kim, Chris Hallacy, Aditya Ramesh, Gabriel Goh, Sandhini Agarwal, Girish Sastry, Amanda Askell, Pamela Mishkin, Jack Clark, et al. Learning transferable visual models from natural language supervision. In *International Conference on Machine Learning*, pages 8748–8763. PMLR, 2021. [2](#), [3](#)
- [22] Shashank Tripathi, Agniv Chatterjee, Jean-Claude Passy, Hongwei Yi, Dimitrios Tzionas, and Michael J Black. Deco: Dense estimation of 3d human-scene contact in the wild. In *Proceedings of the IEEE/CVF International Conference on Computer Vision*, pages 8001–8013, 2023. [2](#)
- [23] Yuxiao Wang, Qi Liu, and Yu Lei. TED-Net: Dispersal attention for perceiving interaction region in indirectly-contact hoi detection. *IEEE Transactions on Circuits and Systems for Video Technology*, 2024. [1](#), [2](#)
- [24] Yisen Wang, Yao Teng, and Limin Wang. CycleHOI: Improving human-object interaction detection with cycle consistency of detection and generation. *arXiv preprint arXiv:2407.11433*, 2024. [2](#)
- [25] Yuxiao Wang, Zhenao Wei, Xinyu Jiang, Yu Lei, Weiying Xue, Jinxiu Liu, and Qi Liu. Freea: Human-object interaction detection using free annotation labels. *arXiv preprint arXiv:2403.01840*, 2024. [1](#), [2](#)
- [26] Yuxiao Wang, Qiwei Xiong, Yu Lei, Weiying Xue, Qi Liu, and Zhenao Wei. A review of human-object interaction detection. *arXiv preprint arXiv:2408.10641*, 2024. [1](#), [2](#)
- [27] Yuxiao Wang, Wenpeng Neng, Zhenao Wei, Yu Lei, Weiying Xue, Nan Zhuang, Yanwu Xu, Xinyu Jiang, and Qi Liu. Precision-enhanced human-object contact detection via depth-aware perspective interaction and object texture restoration. In *Proceedings of the AAAI Conference on Artificial Intelligence*, 2025. [2](#), [5](#), [7](#), [8](#)
- [28] Chenxia Wu, Jiemi Zhang, Silvio Savarese, and Ashutosh Saxena. Watch-n-Patch: Unsupervised understanding of actions and relations. In *Proceedings of the IEEE conference on computer vision and pattern recognition*, pages 4362–4370, 2015. [6](#)
- [29] Tete Xiao, Yingcheng Liu, Bolei Zhou, Yuning Jiang, and Jian Sun. Unified perceptual parsing for scene understanding. In *Proceedings of the European conference on computer vision (ECCV)*, pages 418–434, 2018. [7](#)
- [30] Jie Yang, Bingliang Li, Ailing Zeng, Lei Zhang, and Ruimao Zhang. Open-world human-object interaction detection via multi-modal prompts. In *Proceedings of the IEEE/CVF Conference on Computer Vision and Pattern Recognition*, pages 16954–16964, 2024. [2](#)
- [31] Lixin Yang, Xinyu Zhan, Kailin Li, Wenqiang Xu, Junming Zhang, Jiefeng Li, and Cewu Lu. Learning a contact potential field for modeling the hand-object interaction. *IEEE transactions on pattern analysis and machine intelligence*, 2024. [2](#)
- [32] Hengshuang Zhao, Jianping Shi, Xiaojuan Qi, Xiaogang Wang, and Jiaya Jia. Pyramid scene parsing network. In *Proceedings of the IEEE conference on computer vision and pattern recognition*, pages 2881–2890, 2017. [7](#)
- [33] Li'an Zhuo, Jian Cao, Qi Wang, Bang Zhang, and Liefeng Bo. Towards stable human pose estimation via cross-view fusion and foot stabilization. In *Proceedings of the IEEE/CVF Conference on Computer Vision and Pattern Recognition*, pages 650–659, 2023. [2](#)
- [34] Cheng Zou, Bohan Wang, Yue Hu, Junqi Liu, Qian Wu, Yu Zhao, Boxun Li, Chenguang Zhang, Chi Zhang, Yichen Wei, et al. End-to-end human object interaction detection with HOI transformer. In *Proceedings of the IEEE/CVF Conference on Computer Vision and Pattern Recognition*, pages 11825–11834, 2021. [2](#)